

Shape-Dependent Field Enhancement and Plasmon Resonance of Oxide Nanocrystals

Ankit Agrawal,[†] Ilka Kriegel,[‡] and Delia J. Milliron*,[†]

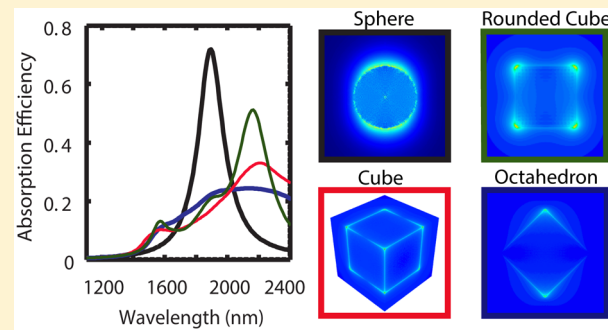
[†] McKetta Department of Chemical Engineering, University of Texas at Austin, Austin, Texas 78712-1589, United States

[‡] Dipartimento di Fisica, Politecnico di Milano, Piazza Leonardo da Vinci 32, 20133 Milano, Italy

Center for Nano Science and Technology@PoliMi, Istituto Italiano di Tecnologia, Via Giovanni Pascoli 70/3, 20133 Milan, Italy

Supporting Information

ABSTRACT: Metallic nanostructures can manipulate light-matter interactions to induce absorption, scattering, and local heating through their localized surface plasmon resonances. Recently, plasmonic behavior of semiconductor nanocrystals has been investigated to stretch the boundaries of plasmonics farther into the infrared spectral range and to introduce unprecedented tunability. However, many fundamental questions remain regarding characteristics of plasmons in doped semiconductor nanocrystals. Field enhancement, especially near features with high curvature, is essential in many applications of plasmonic metal nanostructures, yet the potential for plasmonic field enhancement by semiconductor nanocrystals remains unknown. Here, we use the discrete dipole approximation (DDA) to understand the dependence of field enhancement on size, shape, and doping level of plasmonic semiconductor nanocrystals. Indium-doped cadmium oxide is considered as a prototypical material for which faceted cube-octohedral nanocrystals have been experimentally realized; their optical spectra are compared to our computational results. The computed extinction spectra are sensitive to changes in doping level, dielectric environment, and shape and size of the nanocrystals, providing insight for materials design. High-scattering efficiencies and efficient local heat production make 100 nm particles suitable for photothermal therapies and simultaneous bioimaging. Meanwhile, single particles and dimers of nanocrystals demonstrate strong, shape- and wavelength-dependent near-field enhancement, highlighting their potential for applications in infrared sensing, imaging, spectroscopy, and solar conversion.



INTRODUCTION

The ability to localize electromagnetic waves to the size of the nano object through localized surface plasmon resonances (LSPRs) gives rise to a manifold of applications and biology-related challenges, such as sensing,^{1–7} enhanced spectroscopies,^{8–17} or photothermal therapy.^{4,22,23} In metallic nanocrystals (NCs), the LSPR is mostly limited to the visible part of the spectrum and determined at the stage of synthesis. The LSPR frequency range of metallic nanostructures can be further extended to the near-infrared (NIR), but this requires larger sized particles with complex shapes such as nanorods¹⁶ (>50 nm in length) or nanoshells^{17,18} (>60 nm in diameter). The ability to modify the plasmon resonance of NCs less than 20 nm in size to precise resonant absorption lines and with resonances within the biological window in the NIR¹⁹ would be beneficial for numerous applications, such as enhancement spectroscopies in the near-infrared,^{5,6,20} sensing, or photothermal therapies.^{21,22}

More recently, intense interest has been focused on a new type of plasmonic nanomaterials offering exactly these tunable properties, namely doped semiconductor NCs.^{23,24} These are comprised of vacancy doped semiconductors such as copper chalcogenides,^{25–27} tungsten oxides,^{28,29} or doped metal oxide

nanocrystals.^{23,24,30–32} The greatest advantage is, however, the possibility to tune their plasmonic absorption through a careful choice of the dopant concentration, which establishes the number of carriers and, thus, the spectral position of the LSPR.^{24,33} In metal oxides, synthetic control over doping has been made possible by balancing the reactivity of precursors for the dopant and host crystal. Controlled synthetic doping with precise shape control^{23,24,34} leads to carrier densities in the range of 10^{20} – 10^{21} cm⁻³ and plasmon resonances covering a broad range of frequencies from the red to the infrared spectral range.^{24,35} Moreover, the possibility to postsynthetically modify the LSPR by applying a voltage to conducting films of such NCs has been demonstrated^{33,36–39} and successfully applied to electrochromic devices.^{38,39} More recent work has triggered the implementation of such NCs as sensors for chemical redox reactions, where an electron transfer event can be detected as a shift in the LSPR on a single electron level.⁴⁰ Moreover, in photoredox chemistry, a shift of the plasmon resonance is triggered by photochemical addition of electrons, which can be reversed by the addition of mild oxidants.⁴¹

Received: February 17, 2015

Published: March 5, 2015

Indium-doped cadmium oxide (ICO) is an interesting candidate of such material.³⁰ The great advantage of ICO is that its spectral characteristics can be well-understood by a simple Drude-like free electron model, as demonstrated by analysis of optical spectra of thin films of ICO with different doping levels.^{42,43} Unlike in other doped metal oxides, where impurity scattering results in a frequency dependent damping⁴⁴ or vacancies in the crystal result in localization effects,⁴⁵ the carriers in this material can be considered as essentially free and thus can be treated like a Drude metal.⁴² ICO nanoparticles have been demonstrated to provide a tunable LSPR by varying the doping level and to be synthesized in various shapes such as spheres or octahedra.³⁰ However, many open questions remain, in particular regarding the plasmonic properties of ICO nanoparticles, their shape-, size-, and doping-dependent near- and far-field properties, their sensitivity to the surrounding medium, the possible effects of coupling plasmons in adjacent nanoparticles, and the potential for local heat production by dissipating energy from plasmon excitations. In this work, we explore these characteristics and simulate plasmonic far- and near-field properties of ICO nanoparticles under different constraints.

A powerful tool to unlock these plasmonic properties of ICO NCs is the discrete dipole approximation (DDA).^{46–50} The NC volume is discretized into a finite array of polarizable points on a cubic lattice, and the polarizability is calculated by taking into account the electric field arising from the surrounding induced dipoles.^{46,47} Thus, the extinction (absorption and scattering) cross section of a single NC of arbitrary shape or the electric field surrounding the nanostructure can be calculated.

Here, we have done numerical calculations using the DDA and an analytical solution based on the Mie theory in order to calculate for the first time the plasmonic properties of metal oxide nanostructures and, in particular, ICO NCs of varying carrier concentration, shape, and size. The near- and far-field optical responses of differently shaped ICO NCs have been studied, taking advantage of the experimentally determined dielectric function of ICO at various doping levels as taken from ref 44. Our results demonstrate that such NCs are interesting candidates for infrared plasmonics with the benefit of synthesis and postsynthesis control over their LSPR, allowing a precise tailoring of their plasmonic properties, which demonstrate a high sensitivity to the carrier concentration and shape.

RESULTS AND DISCUSSION

A major differentiation of plasmonic semiconductor NCs versus metallic nanoparticles is the possibility to change the free carrier concentration inside the particle over a wide range, which can be pre- and postsynthetically controlled. This plasmon characteristic, which is unique to this class of materials, allows dynamic modulation of the plasmonic response. Here, we investigated the effect of varying carrier concentration via doping on the optical near- and far-field properties of ICO NCs. We simulated the extinction spectra of 10 nm diameter spherical ICO NCs for carrier concentrations varying from 0.81 to $1.33 \times 10^{21} \text{ cm}^{-3}$ (Figure 1a). The strong resonance in the near-infrared (NIR) is ascribed to the localized surface plasmon resonance (LSPR), which can be tuned from 2250 to 1600 nm, depending upon the carrier concentration. A blue shift of the LSPR is observed with increasing carrier concentration. This result can be understood from the Mie theory where the absorption cross section is given as

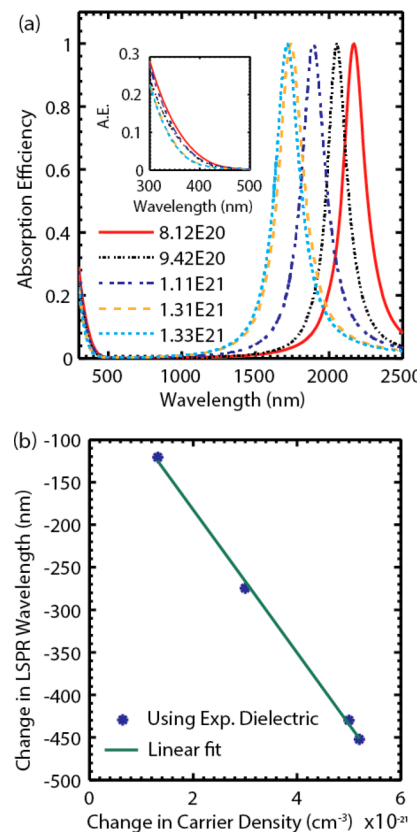


Figure 1. (a) Extinction coefficient of ICO NCs of 10 nm diameter at different levels of doping ranging from 8.1×10^{20} to $1.33 \times 10^{21} \text{ cm}^{-3}$. Inset: interband region illustrating the Moss-Burstein shift with increasing carrier density. (b) Change in LSPR peak wavelength versus change in carrier concentration assuming an initial carrier concentration of $8.12 \times 10^{20} \text{ cm}^{-3}$. The slope of the linear relationship is defined by us as the carrier concentration sensitivity factor.

$$C_{\text{abs}}(\omega) = 4\pi k(\epsilon_H)^{1/2} R^3 \text{Im} \left\{ \frac{\epsilon_p(\omega) - \epsilon_H}{\epsilon_p(\omega) + 2\epsilon_H} \right\} \quad (1)$$

with k being the wavevector, R the NC radius, ϵ_H the host dielectric constant, and $\epsilon_p(\omega)$ the material dielectric function. Taking the resonance condition $\epsilon_r = -2\epsilon_H$ and the Drude dielectric function, the LSPR peak position can be found as

$$\omega_{\text{LSPR}} = \sqrt{\frac{\omega_p^2}{1 + 2\epsilon_H} - \gamma^2} \quad (2)$$

where γ is the damping constant and ω_p the plasma frequency that relates the carrier density, N_c , to the LSPR peak position ω_{LSPR} is

$$\omega_p = \sqrt{\frac{N_c e^2}{m_e^* \epsilon_0}} \quad (3)$$

where e is the electron charge, m_e^* is effective electron mass, and ϵ_0 is the vacuum permittivity.

Thus, an increase in carrier density directly explains the strong blue shift of the plasmon peak position. In line with this, it has been shown in a recent work by Mendelsberg et al.⁴⁰ that using the carrier dependent plasmon peak shift, it is possible to track, model, and quantify electron transfer events from organic, inorganic, biogenic, and even living species to the

doped semiconductor NC. To quantify the sensitivity of the plasmon peak to the actual carrier concentration N_c , we have derived the carrier concentration sensitivity factor (S_{N_c}) using the Drude model and the Mie theory (the derivation is given in the Supporting Information). The carrier concentration sensitivity factor linearly correlates the change in the LSPR peak ($\Delta\lambda$) to the change in free carrier concentration (ΔN_c) as shown below.

$$\Delta\lambda = -S_{N_c}\Delta N_c \quad (4)$$

where

$$S_{N_c} = \frac{\lambda_i^3 e^2}{2m_e^* \epsilon_o (\epsilon_\infty + 2^* \epsilon_H) c^2} \quad (5)$$

λ_i is the initial plasmon peak, ϵ_∞ is the bulk high frequency dielectric constant, and c is the speed of light (all in SI units). ICO NCs with an initial carrier density of $0.81 \times 10^{21} \text{ cm}^{-3}$ follow this correlation precisely, having a sensitivity factor of $20 \text{ nm}/10^{20} \text{ cm}^{-3}$ (Figure 1b). This means that for a spherical ICO NC of 5 nm in diameter, the addition of 100 electrons would lead to a shift of the plasmon resonance of 38 nm. The addition of even one electron would give an easily detectable shift of 3.8 nm, underscoring the potential of these NCs as highly sensitive redox sensors.

Since our calculations have been performed using an experimentally measured dielectric function⁴¹ which inherently includes the contribution of interband transitions, we can see the onset of the interband absorption in all spectra at around 450 nm, which is blue-shifted with respect to the bulk bandgap of undoped CdO at around 570 nm (2.16 eV).⁵¹ The blue shift of the interband absorption increases progressively with increasing carrier density (Figure 1a, inset). This shift is understood in terms of the Moss-Burstein effect of heavily doped semiconductors, where the optical band gap is shifted to higher energy due to the filling of states near the conduction band edge with increasing doping level.⁵²

Another very important characteristic of plasmonic NCs is the ability to efficiently scatter light resonant with the plasmon frequency. We calculated the extinction spectra of ICO NCs of varying size, ranging from 10 to 300 nm in diameter (Figure 2a). In the far-field response with increasing size up to around 100 nm in diameter, no change in the plasmon peak position is observed and a change in peak intensity is consistent with the increase in absorption with the volume change. In this size regime, absorption is the dominant mechanism contributing to the extinction, and scattering is almost completely absent. These calculations are consistent with the dipolar approximation of the Mie theory for particles very small in comparison to the incoming wavelength.⁵³ From particles of 100 to 300 nm in diameter, we observe a red-shifted plasmon resonance and the contribution of scattering increases rapidly, so that scattering is stronger than absorption for the 300 nm diameter particles (Figure 2b). This very strong plasmon scattering in the infrared is a distinguishing characteristic of doped semiconductor NCs and is envisaged to be very useful for application such as infrared microscopy,⁵⁴ imaging,⁴ or enhanced solar conversion.⁵⁵ As sizes increase toward the electromagnetic field decay length, asymmetry in the extinction spectrum is observed and multimode absorption arises (Figure 2b). The origin of these modes is explored by calculating the spatial distribution of the electric near field.

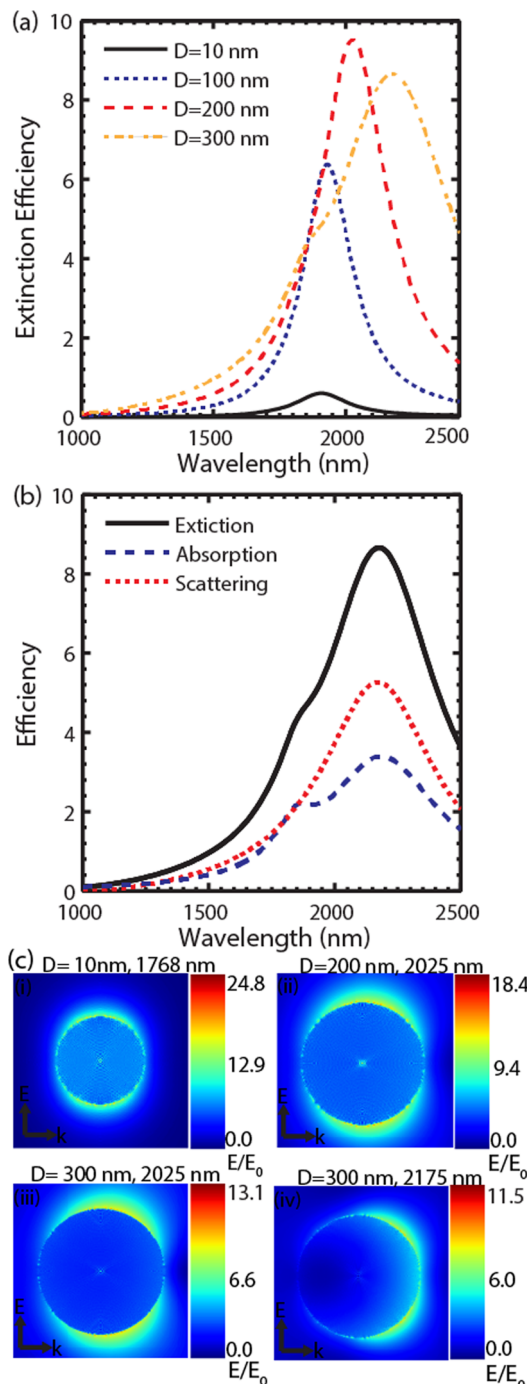


Figure 2. (a) Extinction spectra of spherical ICO NCs of increasing diameters ranging from 10 to 300 nm. (b) The scattering (red) and absorption (blue) contribution to the extinction of a 150 nm diameter sphere. For sizes of less than 100 nm, the scattering becomes negligible (not shown here). (c) NFE maps for the same NCs with increasing size. (i) The NFE factors are not influenced by size in a range from 10 to 100 nm in diameter (see the Supporting Information). (ii) NFE becomes lower because scattering and multipolar modes start to play a major role for 200 nm diameter particles. (iii and iv) NFE maps illustrating the multipolar modes for the 300 nm sized NC.

Maps of the enhanced electric near-field under variable single-wavelength excitation are calculated for NCs of 10, 200, and 300 nm diameter to reveal the plasmon modes responsible for the far-field resonance peaks (Figure 2c). Below 100 nm, isolated spherical NCs have dipolar modes with modest near

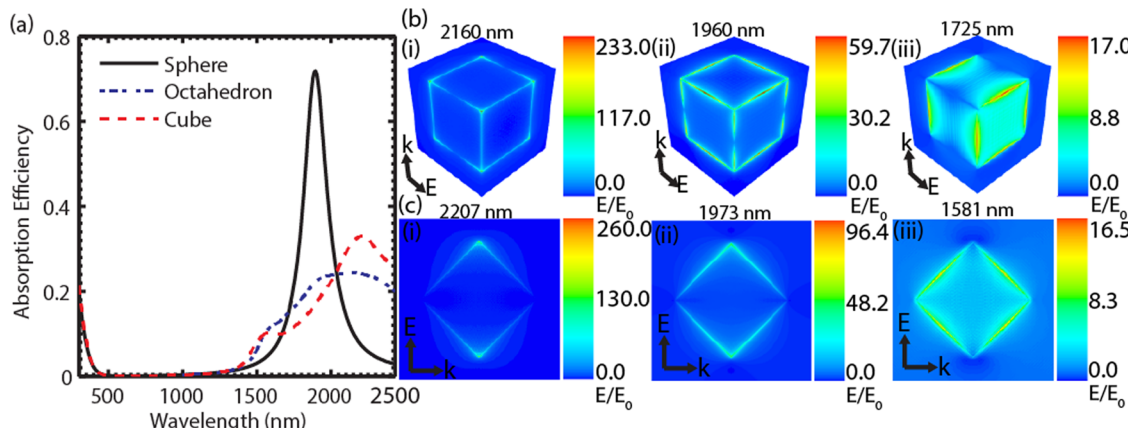


Figure 3. (a) Extinction spectra of differently shaped ICO NCs with a carrier density of $1.11 \times 10^{21} \text{ cm}^{-3}$: all shapes have volume equivalent to volume of a 10 nm spherical particle. The spectra of cube and octahedron are dominated by multiple peaks. (b) NFE map of cube excited at 2160, 1960, and 1725 nm demonstrating the multipolar excitation. For the highest intensity peak (2207 nm), the enhanced field is strongly localized at the corners of the cube, reaching field enhancement factors of up to 233, while for the lower intensity peaks the field enhancement is spread over the edges (1960 nm) and faces (1725 nm) leading to decreased enhancement factors. (c) NFE map of octahedron excited at 2207, 1973, and 1581, demonstrating the multipolar modes. For the highest intensity peak (2160 nm), the enhanced field is strongly localized at the corners of the octahedron, reaching field enhancement factors of up to 260, while for the lower intensity peaks the field enhancement is spreading over the edges (1973 nm) and faces (1581 nm) leading to decreased enhancement factors.

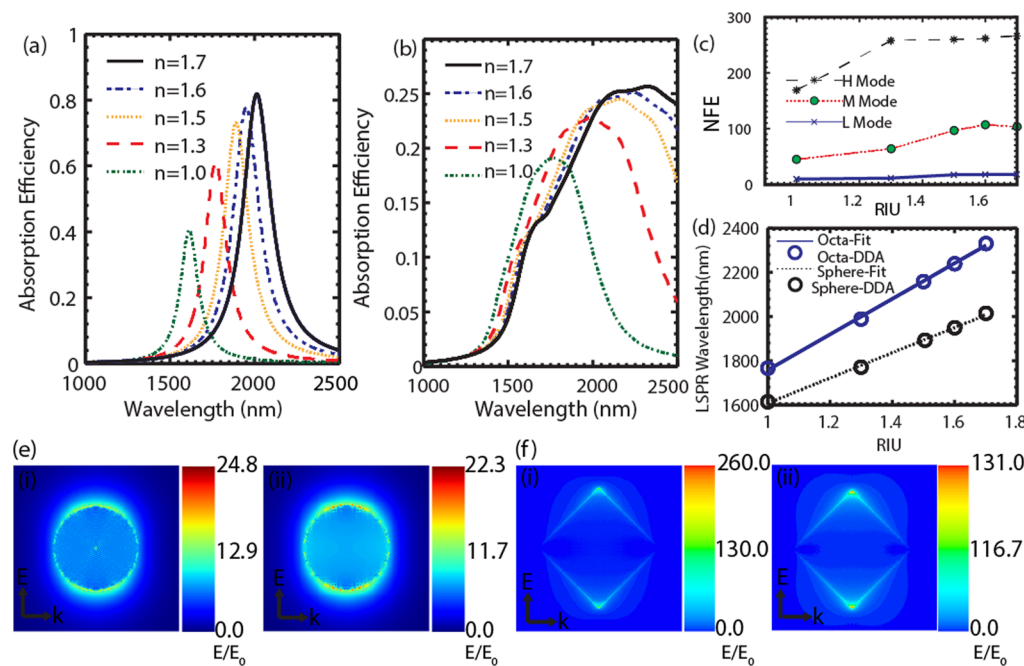


Figure 4. Extinction spectra of (a) sphere of 10 nm diameter and (b) octahedron with volume equivalent to volume of 10 nm spherical particle and a carrier density of $1.11 \times 10^{21} \text{ cm}^{-3}$ in different medium refractive index. A red shift and increase in intensity is observed with increasing surrounding refractive index. (c) NFE factors excited at the highest intensity absorption peak (H Mode), mid intensity peak (M mode), and low intensity peak (L mode) versus refractive index of the medium. (d) LSPR peak wavelength versus refractive index for both spherical and octahedron particle. All calculations were performed with the experimental dielectric functions, and the fits show linear correlation as expected from the sensitivity relation (eq 6) and (f) NFE maps for different carrier densities of (i) $9.42 \times 10^{20} \text{ cm}^{-3}$, (ii) $1.11 \times 10^{21} \text{ cm}^{-3}$ for the (e) sphere and the (f) octahedron. With increasing carrier density, the NFE is increasing.

field enhancement (NFE) factors up to 24. The NFE is independent of the NC size for sizes up to 100 nm, consistent with the Mie theory in the dipolar regime (Figure 2c (i) and Figure S3 in the Supporting Information).⁶ As scattering makes a stronger contribution for the 200 nm diameter particle, the NFE starts to decrease [Figure 2c (ii)]. We can also clearly see the effect of electric field decay along the wave vector in the 300 nm particle spectra and that the higher intensity peak is due to the dipolar mode and the lower intensity peak is due to the quadrupole mode [Figure 2c (iii and iv)]. These results show that plasmonic modes are size dependent above 100 nm, and the relative contribution of absorption and scattering to the total extinction cross section can be tuned by changing the size of the NC.

By varying the growth conditions, differently shaped NCs of the same material can be synthesized. Shape is known to strongly influence the near and far field properties of conventional plasmonic nanomaterials.^{4,12,28,30} In a recent

work by Gordon et al., ICO NCs have been successfully synthesized in different shapes such as sphere and octahedron, and a shape-dependent optical response has been demonstrated.³⁰ Similarly, Mattox et al. reported shape-dependent far-field spectra for Cs_xWO_3 NCs.²⁸ We calculated the shape-dependent extinction spectra for spheres, cubes, and octahedra (Figure 3a). As we move from the spherical to the sharp cornered or edged particles such as the octahedron or cube, the plasmon peak red shifts, becomes broader, and substantially decreases in peak intensity. Moreover, the spectra are characterized by secondary peaks and shoulders corresponding to multipolar excitations.

The origin of the multiple peaks can be explained using near-field calculations on faceted NCs. In the calculations, the plasmon resonance is excited at the different peak or shoulder wavelengths with light polarized in the y direction, and the NFE of the electric field is calculated. The NFE maps of the octahedron show multipolar modes mostly distributed over the faces, the edges, and the corners (Figure 3c). The distribution of the near field is primarily over the faces when exciting the lowest intensity peak (1725 nm), over the edges when exciting the mid intensity peak (1960 nm), and over the corners for the highest intensity peak (2160 nm), leading to NFE factors between 16.5 and 260. The strong differences in intensity are understood by the different distributions of the field. The strong accumulation of field intensity at the corners for excitation with the highest intensity peak leads to the highest NFE factors of up to 260. Very similar results are observed for the cubic particle, where the shift of the accumulated near field from the faces to the corners results in increased NFE factors of up to 233 (Figure 3b). The higher NFE factor in the octahedron with respect to the cube is due to excitation polarization along tip–tip diagonal. These strongly localized field distributions are responsible for high sensitivity of the plasmon resonance to the refractive index of the surrounding medium, and this sensitivity is exploited for various applications such as sensing of single molecules or mass spectrometry.^{5,6,54} An advantage that our semiconducting nanoparticles hold over metallic ones is their surface chemistry that supports surfactants of various functional groups and coordination chemistry for specific binding to certain facets in the crystal. The surface chemistry of semiconducting nanoparticles has been studied in detail and is widely understood, resulting in the possibility to fine-tune and precisely control the shape and size of such nanoparticles.^{56–58} Thus, a direct attachment of various functional groups to specific facets is given in semiconducting NCs, which can be exploited for sensing application or surface-enhanced spectroscopies with site-specific detection.⁵⁹

To analyze the sensitivity of our nanostructures to their surrounding medium, we have calculated the plasmon resonance of ICO nanoparticles with different surrounding refractive index, thereby taking into account differently shaped particles, such as sharp cornered octahedra, cubes, or spherical particles. First, we have calculated the plasmonic response for a 10 nm diameter spherical particle to the medium refractive index (Figure 4a) using the Mie theory, which in the dipolar limit gives similar results to the DDA (see also Figure S1 of the Supporting Information). Equation 6 demonstrates the dependence of the absorption to the surrounding medium:

$$\Delta\lambda = m\Delta n \quad (6)$$

where m is the sensitivity factor per refractive index unit, Δn is the change in refractive index, and $\Delta\lambda$ is the corresponding

wavelength shift.⁵ The calculated extinction spectra for the sphere (Figure 4a) show an increase in peak intensity and a red shift with increasing refractive index. For sensing application, it has been found that sharp edges or corners in the plasmonic nanoparticles give a stronger response to changes in the surrounding environment.⁶⁰ Thus, we calculated the shape-dependent response of the ICO octahedron to changes in the surrounding medium (Figure 4b). A redshift in plasmon peak is observed with increasing refractive index of the medium, which is greater in magnitude compared to the spherical particle (Figure 4d). Using eq 6 and from Figure 4d, we have calculated the sensitivity factor per refractive index unit for both spherical and octahedron particles at their highest intensity peaks to be 560 and 804 nm per refractive index unit (RIU^{-1}), respectively, demonstrating the stronger sensitivity of the ICO octahedron and spherical particle to the medium refractive index when compared to a typical RIU of around 300 nm for gold nanorods.⁶¹ This sensitivity in turn affects the NFE factors as summarized for the three peaks of the octahedron in Figure 4c, demonstrating an increase of NFE with increasing refractive index. This is understood due to the weaker electric field in a medium with higher refractive index. Generally, our results demonstrate that each mode separately shows sensitivity to the medium refractive index, which implicates that a control over specific binding to the NC surface is of great importance for molecular sensing applications or enhanced spectroscopies in the infrared.

The NFE is also strongly dependent on the carrier concentration. Therefore, we calculated the NFE maps for both the sphere and the octahedron (Figure 4, panels e and f) for two different carrier densities of (i) $9.42 \times 10^{20} \text{ cm}^{-3}$ and (ii) $1.11 \times 10^{21} \text{ cm}^{-3}$. As we increase the free carrier density, the NFE factor increases. While this effect is minor in the sphere, it is very strong for the octahedron (from around 130 to around 260). This result goes in hand with a stronger sensitivity of the plasmon resonance to the surrounding medium of the NC (due to the higher fields). We envisage that the in situ tuning of the NC carrier density could modify the sensitivity of the plasmon resonance to its surrounding. Thus, a variation of the NFE through the control of the carrier concentration in the NCs offers a way to switch on, off, and fine-tune its sensitivity to the surrounding, supplying an additional parameter for resonance-specific sensing. Taken together, the carrier density, size, shape, and refractive index deliver a broad variety of parameters to tune the near and far field properties of ICO NCs in the near-infrared, with a more complex shape and higher carrier density delivering higher NFEs.

Thus, far, perfectly shaped NCs have been considered; however, realistic NCs have rounded edges that may influence plasmonic properties. To explore the impact of such shape perturbations in ICO NCs, we compared the ensemble extinction spectra of synthesized ICO octahedra NCs with our calculations. By transmission and scanning electron microscopy (TEM and SEM) of the octahedral NCs (Figure 5a, inset), it is observed that the 10–20 nm sized particles show a strong deviation from a perfect shape, in that the edges and corners are rounded in most cases. The experimental absorption spectrum is qualitatively similar to the calculated spectrum for an isolated, perfect octahedron, but the experimental spectrum is not as broad as the simulated one (Figure 5a). This difference motivated us to study with the DDA the effect of rounding of the corners and edges on the absorption spectra and NFE. This study was performed on a

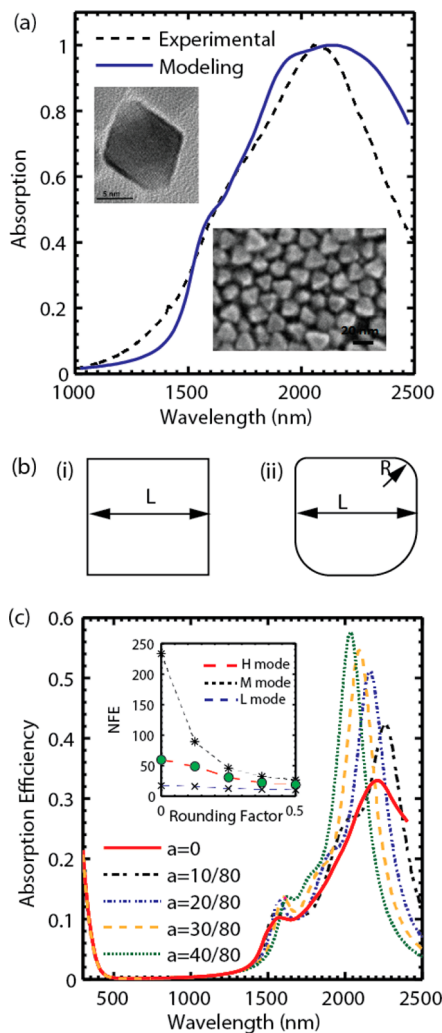


Figure 5. (a) Experimental and theoretical absorption spectra of around 10 nm ICO octahedron particle (insets) TEM and SEM images of synthesized octahedral particles show a deviation from the perfect octahedron shape due to rounding of the edges and corners. (b) Illustration of rounding of the edges and corners of a perfect cube (i) to different extents as illustrated by the different rounding of the four corners (ii). The value of (a) defines the rounding as is calculated by $a = R/L$. (c) Effect of rounding the edges and corners of a cube with a carrier density of 1.11×10^{21} on the absorption spectrum. Volume of all the shape is equivalent to volume of 10 nm spherical particle. Inset: the NFE factor versus rounding. With increasing rounding, the different modes merge together to reach an unresolved broad band, along with a dramatic decrease in NFE factors.

cubic particle of an 8 nm side length. To study this effect, the corners and edges of a perfect cube [Figure 5b, (i)] are rounded to a different extent [Figure 5b (ii)]. The rounding has been described using a rounding factor (a) as the ratio between the radius of curvature (R) to the side length of the perfect cube (L). The calculated extinction spectra for the perfect cube of an 8 nm dimension is shown in Figure 5c, together with four rounded edge cubes. As we increase the rounding, the highest intensity peak blue shifts and the spectrum becomes narrower. Lower- and higher-order modes move toward each other as rounding increases, and the most intense dipolar mode⁶² dominates the absorption spectra approaching the single dipolar mode of a perfect sphere. These simulations are consistent with the experimental observation for the 10–20 nm

sized octahedra (Inset, Figure 5a), where a more narrow resonance was found in the synthesized NCs, with lower- and higher-energy modes that are closer in energy compared to the spectrum calculated for the perfect octahedron. From NFE calculations, we can see that as we increase the rounding, there is a significant decrease in the enhancement from 233 for the perfect cube (highest intensity mode) to 69.4 for a rounding of 1/8. NFE maps for different rounding factors are shown in Figure S2 of the Supporting Information. These results demonstrate that for any application based on near field enhancement, the synthetic route should be optimized to have maximally precise shape control.

Other than developing new synthetic routes, coupling of plasmonic particles arranged in assemblies may offer another option to reach higher enhancement factors. Indeed, in our calculations a sharp increase in the NFE occurs via the formation of hot spots in between proximal particles (see below). A major application taking advantage of the high NFE factors is surface-enhanced Raman spectroscopy (SERS). It has been found that as a molecule is adsorbed onto a plasmonic nanoparticle or comes close to it, the Raman scattering gets enhanced by factors ranging from 10^8 to 10^{14} .^{6,9,10} This leads to specific and sensitive detection of molecules. To get the maximum enhancement, it is ideal to have the plasmon wavelength close in energy to both the incident wave frequency and the Stokes shifted Raman frequency.⁶ Another way to enhance the Raman signal is resonance Raman spectroscopy, where the Raman signal is enhanced at least by 5 orders of magnitude (SERRS), when exciting with a laser in resonance to an electronic transition of the molecule.⁶³ In addition, surface-enhanced infrared spectroscopy leads to enhanced infrared absorption signals of molecules covering islands of plasmonic nanostructures that show plasmonic absorption up to the infrared.⁶⁴ Plasmonic semiconductor NCs have plasmonic resonances in the infrared tunable over a broad range of wavelengths. This might deliver a new approach to enhanced spectroscopies in the infrared through a pre- or postsynthetic fine-tuning of the LSPR peak to the frequencies of interest, such as the molecular resonance of a certain molecule of desire.

Thus, we investigated the field enhancement between adjacent plasmonic ICO NCs with spherical shape, tip-to-tip enhancement in octahedron NCs and face-to-face enhancement in cubic NCs. These orientations could plausibly be formed during assembly of NCs. Absorption spectra were calculated for a polarization parallel (x -polarized) and perpendicular (y -polarized) to the center-to-center axis of the dimer (here the x axis). The effect of coupling was studied for different interparticle distances a , defined as a factor of the maximum particle dimension D along the x axis, as illustrated in Figure 6 (panels a–c), upper panel. The calculated absorption spectra vary with the value of a for the spherical, octahedron, and cubic NC dimers excited with x -polarization (along the dimer axis, Figure 6, panels a–c). As the interparticle distance decreases and the coupling becomes stronger, the major plasmon peak red shifts for all shapes, which becomes very pronounced with an interparticle distance of 0.2 D and less. For particles in direct contact ($a = 0$), or nearly so ($a = 0.01$ D), a stronger effect is observed: in the sphere and the cube dimer, the absorption spectrum changes drastically with strong multimodal peaks appearing (Figure 6a). This is attributed to the occurrence of new plasmon modes distributed over the entire NC dimer. Since in the case of the tip-to-tip octahedron dimer, the

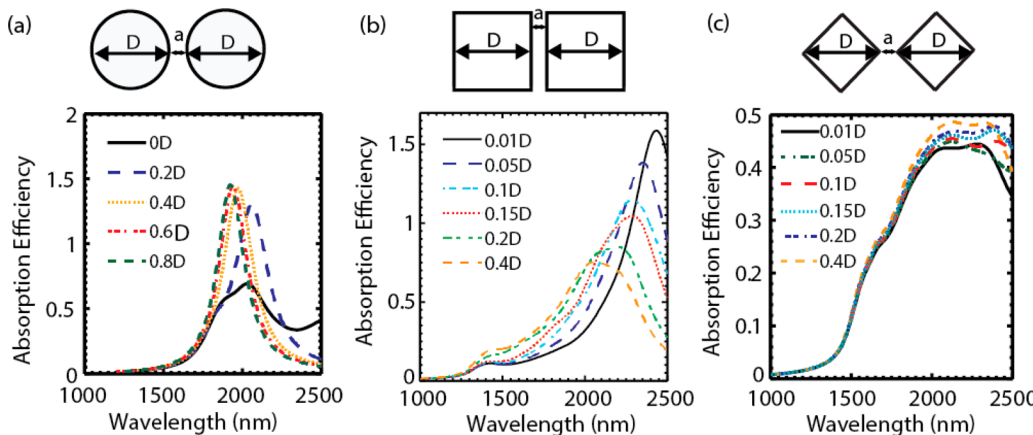


Figure 6. (a) Absorption spectra for the dimers of (a) sphere, (b) cube, and (c) octahedron for different interparticle distances a and a carrier density of $1.11 \times 10^{21} \text{ cm}^{-3}$ for sphere and octahedron and $1.3 \times 10^{21} \text{ cm}^{-3}$ for the cube dimer. Volume of a single particle in all the dimers are equivalent to the volume of 10 nm spherical particle. LSPR shifts due to interparticle plasmon coupling the closer the particles get. This effect is the strongest in the cube dimer with face-to-face orientation.

plasmon coupling region is very small, we do not observe a very pronounced effect on its spectra, even for near-direct contact.⁶⁵

The strong plasmon coupling in NC dimers also leads to the generation of hot spots in the NC dimer gap. The NFE factors are increased multifold in the zone between the particles and are increasing with decreasing interparticle distance. The maximum enhancement was found for interparticle ratios between $a = 0.05$ and 0.2 . A coupling analysis for the ratios from 0 to 0.05 has been omitted, as the classical Maxwell treatment fails in this zone and quantum tunneling effects take over.⁶⁵ NFE maps were calculated for sphere, cube, and octahedron dimers for different interparticle distances (Figure 7, panels a–c). The closer the NCs, the higher the NFE factors become (Figure 7a). In the sphere and octahedron dimers, a clear hot spot between the two particles is observed [Figure 7c (i) and (ii), respectively]. In the case of the cube dimer, the location of the maximum field enhancement is strongly dependent on the distance between the particles (Figure 7b). For cubes very close to each other (i.e., less than 0.1 D), the enhancement is very much localized in between the faces, while the enhancement shifts toward the corners as the distance increases. Similar results were observed previously for the case of gold nanoparticles.⁴⁸ For the excitation of the dimer, we chose the highest intensity peak in all cases, while we note that the enhancement at the lower energy plasmon peak in the cube dimer is very similar to that of the higher energy peak (see Figure S5 of the Supporting Information). For y-polarized light (perpendicular to the dimer axis), coupling was very weak and minor changes to the absorption spectra were observed for all the shapes (Figure S6 of the Supporting Information). For distances greater than 1 D, the NC plasmon characteristics approach those of isolated NCs, indicating that for a pronounced coupling effect the interparticle distance ratio needs to be less than 0.2 . Summarizing the maximum NFE versus interparticle distance for all three shapes (Figure 7a), a maximum enhancement of 400 is found in the octahedron case with an interparticle distance of 0.01 D due to the very localized fields between the tips of the octahedron corners. In the small size range investigated here, the spectra and the NFE of the dimers were found to be independent of the size of the NCs and only depended on the relative interparticle distance (Figure S3 of the Supporting Information). This scale-independence has been found previously also for noble metal NCs.⁶⁵

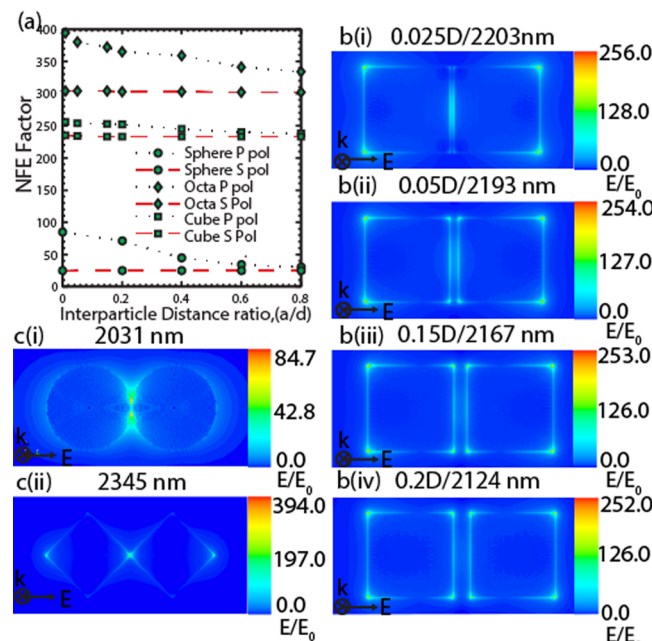


Figure 7. (a) Maximum NFE values versus interparticle separation for the sphere, octahedron, and cube dimers. With decreasing separation, the NFE increases. The highest values of 394 are obtained for the octahedron dimer due to the strong localization of the field between the tips. (B) Coupling in the cube dimer for different interparticle distances ranging from 0.05 D (top panel) to 2 D (bottom panel). The position of the hot spot shifts from between the faces to the corners with increasing distance. (C) Field enhancement map of the (i) sphere and (ii) octahedron dimer with an interparticle distance of 0 D excited at 2031 and 2345 nm, respectively. Hot spots in between the particles are observed, which are strongly localized in the octahedron dimer.

Nevertheless, our results demonstrated that with a clever choice of shape and interparticle distance, we can design a system where field enhancement is obtained at the corners, faces, or in between the spheres, which we predict will allow an enhancement of molecules located at specific facets of plasmonic semiconductor NCs.

Plasmon resonances in NCs are known to decay through the emission of phonons to the surrounding medium and the efficient generation of heat in the local environment.^{56,67}

Currently, plasmonic NCs made of noble metals are being explored for their use in tumor cell cancer treatment,^{14,15} where the heat transfer from the excited NC is used to destroy the cancer cell. To reduce the absorption of the excitation light by the biological medium and associated nontargeted heating effects, researchers are currently trying to shift the plasmon resonances of noble metal NCs toward the infrared zone and into the biological window through synthesis of complex shapes such as gold rods⁶⁸ or nanoshells.⁶⁹ Here, semiconductor NCs are an attractive alternative due to their plasmon resonance inherently in the infrared zone and easily tunable over a wide range of frequencies without resorting to large sizes that can limit biological targeting opportunities. Due to these reasons, semiconductor plasmonic NCs may hold immense potential for biological applications. Important parameters essential in photothermal application are the temperature at the surface of the NC and the light scattering from the NC for possible simultaneous bioimaging. Therefore, we have studied the effect of the NC size and intensity of a monochromatic laser with a frequency equal to the LSPR on the surface temperature of ICO NCs. All the calculations have been performed in steady state. A detailed calculation of the surface temperature can be found in the theory section of this paper. The surface temperature is proportional to the square of the particle radius and to the intensity of the incoming laser light (eq 7, below).

$$(T_{\text{nano}} - T_{\text{bulk}}) = \frac{k_e H R^2}{k_s} \frac{c E_0}{2} |E_0|^2 \text{Im} \left\{ \frac{\epsilon_p(w) - \epsilon_H}{\epsilon_p(w) + 2\epsilon_H} \right\} \quad (7)$$

where T_{nano} is the surface temperature of the nanoparticle, T_{bulk} is the surrounding temperature, k_s is the thermal conductivity of surrounding medium, and E_0 is the incident electric field.

For particles of diameter 20 to 100 nm and an incoming laser intensity of 10^5 W/cm^2 , a local temperature increase of 1 to 20 K can be reached (Figure 8a). This temperature difference can be strongly influenced by choosing the proper laser intensity, as demonstrated in Figure 8b for a 60 nm diameter spherical NC. Our results show that the generation of heat in semiconductor NCs can compete with the properties of noble metal nanoparticles. Semiconductor NCs produce slightly less temperature increase compared to metal nanoparticles which can create temperature rises up to 50 K for similar shapes and sizes.⁶⁶ However, doped metal oxide NCs deliver the unique opportunity of carrying an LSPR in the near-infrared spectral region, even in very small particles, which helps in minimizing light extinction by intrinsic chromophores in tissue¹⁶ and presents an opportunity to design an optimal system for photothermal applications.

CONCLUSIONS

In summary, we have shown that the near- and far-field infrared plasmonic properties of semiconducting ICO NCs are tunable by size and shape, but more importantly, through the variation of the free-carrier concentration, a characteristic unique to doped metal oxide NCs. Thus, for sensors and new optical technologies particularly located in the infrared, these heavily doped semiconductor nanostructures provide an extra degree of freedom for their design and optical integration. This opens the entire new realm of opportunities for an on-device tunability of the infrared LSPR. To quantify this effect and facilitate comparisons between emerging plasmonic materials, we have

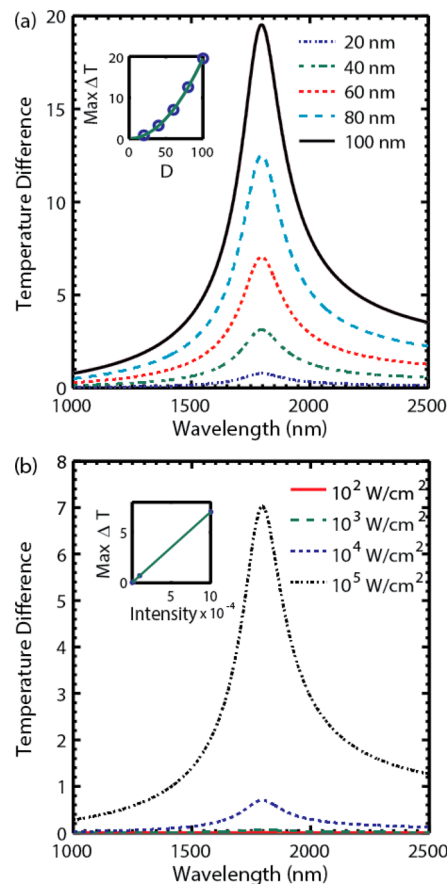


Figure 8. (a) Maximum temperature difference plotted against wavelength for different diameters of spheres ranging from 20 to 100 nm for an excitation density of 10^4 W/cm^2 and a carrier density of 1.11×10^{21} . Inset: The maximum peak temperature difference, ΔT , is directly proportional to the square of the radius of particle (b) for different intensities of the incoming light ranging from 10^2 to 10^5 W/cm^2 for a NC radius of 60 nm. Inset: The maximum peak temperature difference, ΔT , is directly proportional to the intensity of the incident light. With increasing NC size and excitation density, higher temperatures are reached.

defined the carrier concentration sensitivity factor relating the LSPR shift to the change in carrier concentration. In ICO, this factor predicts a peak shift of 3.8 nm upon addition or removal of one electron from a 5 nm NC.

Although metal nanostructures can be designed to have infrared resonance, this has required the use of complex shapes such as nanoholes⁷⁰ or nanoshells¹⁸ and large particles ($>100 \text{ nm}$), which has been a major bottleneck for the development of infrared plasmonics. Applications such as surface-enhanced infrared absorption (SEIRA),⁶⁴ a spectroscopy technique used for applications ranging from studies of catalytic processes to molecular sensing, are limited currently by the limitations in concentrating infrared light into highly localized near fields, which we have now shown is feasible with plasmonic semiconductor NCs. Unlike nanofabricated complex patterns, these NCs are simple to fabricate on a large scale using solution phase synthesis and our calculations predict that they can offer substantial near field enhancement of up to 260 times and high sensitivity to the surrounding medium of up to 800 nm per RIU, all from a very small octahedron nanocrystal (10 nm) and in the infrared regime. These LSPR characteristics represent a substantial opportunity not afforded by conventional metals.

We furthermore found a very strong plasmon scattering contribution of ICO NCs in the infrared from sizes of 100 nm, which is an important parameter for scattering-based application. Taking a cue from experimentally synthesized ICO NCs and their absorption spectra, a study of the edge and corner rounding of cubic NCs showed a tremendous decrease in their NFE properties upon rounding, signifying that for single molecule detection and identification, a precise control over the shape is desired to reach the NFE factors of up to 260 as calculated for perfect octahedra. We demonstrated that “hot spot” dimer-based applications, such as enhanced spectroscopies, as well as photothermal heat transfer, can be extended well in the infrared zone using ICO NCs. For both isolated NCs as well as in dimers, high NFE factors of up to 400 have been found, directly correlating with the spectroscopy-enhancement effectiveness of these infrared plasmonic NCs. While we demonstrated the potential of ICO NCs for infrared plasmonic applications, there are further contributions likely to affect the plasmonic near- and far-field properties, such as the dopant distribution within the particle or the anisotropy of the underlying crystal structure, which are features unique to semiconductor NCs. But nevertheless, with semiconductor plasmonics, we are no more restricted to submicron length scale for infrared plasmonics based applications and instead can concentrate long wavelength far field light into very small regions. Taken together, we believe that with the developing and increasing interest of the scientific community in infrared semiconductor NC plasmonics, breakthrough inventions in the field of sensing, imaging, and spectroscopy in the infrared spectral region will advance rapidly.

THEORY

Lorentz-Mie Theory. The Mie solution is an analytical solution to the Maxwell's equations to obtain light scattering from a spherical particle. It is a general solution for any spherical size and has been simplified under sub wavelength conditions ($a_{\text{eff}} \ll \lambda$). In this quasi-static limit, Mie theory assumes that the phase retardation and effect of higher multipoles are neglected and the field can be considered as constant throughout the volume of the particle. Under this assumption, absorption coefficient is given by the following equation,

$$C_{\text{abs}}(w) = 4\pi k(\epsilon_H)^{1/2} R^3 \text{Im} \left\{ \frac{\epsilon_p(w) - \epsilon_H}{\epsilon_p(w) + 2\epsilon_H} \right\} \quad (8)$$

where k is the wavevector in vacuum, $\epsilon_p(w)$ is the dielectric function of the particle, ϵ_H is the dielectric function of the medium, and R is radius of the particle.

Discrete Dipole Approximation. The Mie solution is only applicable for spherical particles and for ellipsoids or rods applying certain corrections. But in order to simulate extinction spectra for any general shape and size, a numerical method is required. In this work, our computational results are based on a numerical solution of Maxwell's equations. The discrete dipole approximation (DDA) was employed as a numerical method for its solution^{46,47} and an open source program DDSCAT 7.2^{46,47} was employed for the calculation. The DDA technique allows the calculation of the optical absorption and scattering of NCs of arbitrary shape. In practice, the continuum target is approximated by an array of polarizable points located on a cubic lattice with an interdipole distance, d , given by $V = Nd^3$, where V is the volume of the particle and N the number of

polarizable points. The size of the particle is determined by the effective radius $r_{\text{eff}} = (3V/4\pi)^{1/3}$, representing the radius of a sphere of equal volume. The differently shaped NCs are discretized into an $N \times N \times N$ array of interacting spherical dipoles. In order to get converged numerical results, a sufficient number of discrete dipoles needs to be considered, which is chosen to satisfy the convergence condition

$$|elkd| < 0.5 \quad (9)$$

where ϵ is the complex dielectric function and $\kappa = (2\pi/\lambda)$ is a wavenumber. Then, the polarization for each dipole is determined by solving $3N$ equations for

$$\sum_{k=1}^N A_{jk} \vec{P}_j = \vec{E}_{\text{inc},j} \quad (10)$$

with $\vec{E}_{\text{inc},j}$ the incident electric field and \vec{P}_j the polarization of the j th dipole. The interdipole interaction term $A_{jk}(j \neq k)$ is a 3×3 matrix given by

$$A_{jk} = \frac{e^{ikr_{jk}}}{r_{jk}} \left[\kappa^2 (\hat{r}_{jk} \hat{r}_{jk} - \tilde{I}) + \frac{i\kappa r_{jk} - 1}{r_{jk}} (3\hat{r}_{jk} \hat{r}_{jk} - \tilde{I}) \right], \quad j \neq k \quad (11)$$

where r_{jk} is the distance between the j and k dipole, \hat{r}_{jk} is the unit vector along r_{jk} , and \tilde{I} is the identity matrix. The self-interacting term A_{jj} is given by

$$A_{jj} = \alpha_j^{-1} \quad (12)$$

where α_j is the complex polarizability of the dipole, which depends upon the material's dielectric function (ϵ_j), the radius of each dipole (r_{eff}), and the surrounding dielectric medium (ϵ_H). It is given by the corrected discretized Clausius-Mossotti equation. It has been found that accuracy of this mathematical formulation can be improved for high dielectric value materials by filtering out the high spatial frequency component. This new corrected dipole is known as filtered couple dipole. Convergence of the different numerical method is compared to analytical Mie solution in Figure S1 of the Supporting Information.

$$\alpha_j = \frac{\alpha^{(\text{CM})}}{1 + D} \quad (13)$$

where, $\alpha^{(\text{CM})}$ is the Claussius Mossotti term given by

$$\alpha^{(\text{CM})} = \frac{3d^3(\epsilon_j^2 - 1)}{4\pi(\epsilon_j^2 + 1)} \quad (14)$$

and D is the correction term given by

$$D = \frac{\alpha^{(\text{CM})}}{d^3} \left[\frac{4}{3}(\kappa d)^2 - \frac{2}{3\pi} \ln \left[\frac{\pi - \kappa d}{\pi + \kappa d} \right] + \frac{2}{3}i(\kappa d)^3 \right] \quad (15)$$

Extinction, absorption, and scattering cross sections can be calculated using the polarizability obtained from eq 13 through,

$$C_{\text{ext}} = \frac{4\pi\kappa}{|E_0|^2} \sum_{j=1}^N \text{Im}(\vec{E}_{\text{inc},j}^* \times \vec{P}_j) \quad (16)$$

$$C_{\text{abs}} = \frac{4\pi\kappa}{|E_0|^2} \sum_{j=1}^N \left[\text{Im}\{\vec{P}_j \times (\vec{\alpha}_j^{-1})^* \vec{P}_j^*\} - \frac{2}{3}\kappa^3(\vec{P}_j \times \vec{P}_j^*) \right] \quad (17)$$

$$C_{\text{ext}} = C_{\text{abs}} + C_{\text{sca}} \quad (18)$$

Now, near the electric field and internal electric field can be calculated through,

$$\vec{E} = \vec{E}_{\text{inc}} + \vec{E}_{\text{scat}} \\ = \begin{cases} \alpha_j^{-1} P_j & \text{dipole, } j \\ E_{\text{inc},i} - \sum_{j \in \text{dipoles}} A_{ij} P_{ji} & \in \text{surrounding discretization} \end{cases} \quad (19)$$

Extinction, absorption, and scattering efficiency, which is directly calculated from DDSCAT is defined as

$$Q_i = \frac{C_i}{\pi a_{\text{eff}}^2}, \quad \text{where } i = \text{ext, scat, abs} \quad (20)$$

Plasmon Heating. The NC absorption of energy due to the plasmon resonance will give rise to a temperature increase of and around the NC. The heat is considered to be localized in close vicinity of the NCs. Since its dimensions are in the nanometer range, the temperature gradient inside the particle can be considered as static and a steady state is reached within a few picoseconds. Here, we therefore estimate only the steady state temperature profile. At steady state, heat is absorbed by the NC (Q_{abs}) and dissipated to the surrounding (Q_{dis}). For the calculation of the absorbed heat, the absorption cross section C_{abs} of the NC is considered. Then Q_{abs} is given as

$$Q_{\text{abs}} = C_{\text{abs}} I = C_{\text{abs}} \frac{(\epsilon_H)^{1/2} c \epsilon_0}{2} |E_0|^2 \quad (21)$$

with c being the speed of light, and Q_{dis} as

$$Q_{\text{dis}} = h a (T_{\text{nano}} - T_{\text{bulk}}) \quad (22)$$

where h is the heat transfer coefficient, a is the surface area, and T_{bulk} determines the temperature in the surrounding medium. The heat transfer coefficient for a spherical particle immersed in a pool of surrounding medium is given by $h = (k_s/R)$, where k_s is the thermal conductivity of the medium and R is the radius of the particle. Taken together, this results in the following equation

$$(T_{\text{nano}} - T_{\text{bulk}}) = \frac{C_{\text{abs}}}{ha} \frac{(\epsilon_H)^{1/2} c \epsilon_0}{2} |E_0|^2 \quad (23)$$

Substituting C_{abs} from Mie theory for the spherical particle, we get

$$(T_{\text{nano}} - T_{\text{bulk}}) = \frac{k \epsilon_H R^2}{k_s} \frac{c \epsilon_0}{2} |E_0|^2 \text{Im} \left\{ \frac{\epsilon_p(w) - \epsilon_H}{\epsilon_p(w) + 2\epsilon_H} \right\} \quad (24)$$

which determines the temperature change in the surrounding medium as a function of the NC radius R . It shows that temperature difference is proportional to the square of the radius of the particle and directly proportional to the intensity of the incoming wave.

ASSOCIATED CONTENT

Supporting Information

Convergence of DDA and NFE maps, and derivation of the sensitivity factor of plasmon peak to carrier concentration. This material is available free of charge via the Internet at <http://pubs.acs.org>.

AUTHOR INFORMATION

Corresponding Author

*E-mail: milliron@che.utexas.edu.

Notes

The authors declare no competing financial interest.

ACKNOWLEDGMENTS

A.A. was supported in part by the U.S. Department of Energy (DOE) through the SBIR program. Additional support is acknowledged from the Welch Foundation (F-1848).

REFERENCES

- (1) Nath, N.; Chilkoti, A. A Colorimetric Gold Nanoparticle Sensor To Interrogate Biomolecular Interactions in Real Time on a Surface. *Anal. Chem.* **2002**, *74*, 504–509.
- (2) McFadden, P. Broadband Biodection: Holmes on a Chip. *Science* **2002**, *297*, 2075–2076.
- (3) Otsuka, H.; Akiyama, Y.; Nagasaki, Y.; Kataoka, K. Quantitative and Reversible Lectin-Induced Association of Gold Nanoparticles Modified with α -Lactosyl- ω -mercapto-poly(ethylene glycol). *J. Am. Chem. Soc.* **2001**, *123*, 8226–8230.
- (4) Lee, K.-S.; El-Sayed, M. A. Gold and Silver Nanoparticles in Sensing and Imaging: Sensitivity of Plasmon Response to Size, Shape, and Metal Composition. *J. Phys. Chem. B* **2006**, *110*, 19220–19225.
- (5) Anker, J. N.; et al. Biosensing with Plasmonic Nanosensors. *Nat. Mater.* **2008**, *7*, 442–453.
- (6) Willets, K. A.; Van Duyne, R. P. Localized Surface Plasmon Resonance Spectroscopy and Sensing. *Annu. Rev. Phys. Chem.* **2007**, *58*, 267–297.
- (7) Sau, T. K.; Rogach, A. L.; Jäckel, F.; Klar, T. A.; Feldmann, J. Properties and Applications of Colloidal Nonspherical Noble Metal Nanoparticles. *Adv. Mater.* **2010**, *22*, 1805–1825.
- (8) Arpin, K. A.; Losego, M. D.; Braun, P. V. Electrodeposited 3D Tungsten Photonic Crystals with Enhanced Thermal Stability. *Chem. Mater.* **2011**, *23*, 4783–4788.
- (9) Campion, A.; Kambhampati, P. Surface-Enhanced Raman Scattering. *Chem. Soc. Rev.* **1998**, *27*, 241–250.
- (10) Nie, S.; Emory, S. R. Probing Single Molecules and Single Nanoparticles by Surface-Enhanced Raman Scattering. *Science* **1997**, *275*, 1102–1106.
- (11) Talley, C. E.; et al. Surface-Enhanced Raman Scattering from Individual Au Nanoparticles and Nanoparticle Dimer Substrates. *Nano Lett.* **2005**, *5*, 1569–1574.
- (12) Eustis, S.; El-Sayed, M. A. Why Gold Nanoparticles Are More Precious than Pretty Gold: Noble Metal Surface Plasmon Resonance and Its Enhancement of the Radiative and Nonradiative Properties of Nanocrystals of Different Shapes. *Chem. Soc. Rev.* **2006**, *35*, 209.
- (13) Xu, H.; Bjerneld, E. J.; Käll, M.; Börjesson, L. Spectroscopy of Single Hemoglobin Molecules by Surface Enhanced Raman Scattering. *Phys. Rev. Lett.* **1999**, *83*, 4357–4360.
- (14) Huang, X.; El-Sayed, M. A. Gold Nanoparticles: Optical Properties and Implementations in Cancer Diagnosis and Photothermal therapy. *J. Adv. Res.* **2010**, *1*, 13–28.
- (15) Huang, X.; Jain, P. K.; El-Sayed, I. H.; El-Sayed, M. A. Gold Nanoparticles: Interesting Optical Properties and Recent Applications in Cancer Diagnostics and therapy. *Nanomedicine* **2007**, *2*, 681–693.
- (16) Huang, X.; El-Sayed, I. H.; Qian, W.; El-Sayed, M. A. Cancer Cell Imaging and Photothermal Therapy in the near-Infrared Region by Using Gold Nanorods. *J. Am. Chem. Soc.* **2006**, *128*, 2115–2120.

- (17) Oldenburg, S. J.; Averitt, R. D.; Westcott, S. L.; Halas, N. J. Nanoengineering of Optical Resonances. *Chem. Phys. Lett.* **1998**, *288*, 243–247.
- (18) Lal, S.; Clare, S. E.; Halas, N. J. Nanoshell-Enabled Photothermal Cancer Therapy: Impending Clinical Impact. *Acc. Chem. Res.* **2008**, *41*, 1842–1851.
- (19) Jaque, D.; et al. Nanoparticles for Photothermal Therapies. *Nanoscale* **2014**, *6*, 9494–9530.
- (20) Kneipp, K.; Kneipp, H.; Itzkan, I.; Dasari, R. R.; Feld, M. S. Ultrasensitive Chemical Analysis by Raman Spectroscopy. *Chem. Rev.* **1999**, *99*, 2957–2976.
- (21) Hessel, C. M.; et al. Copper Selenide Nanocrystals for Photothermal Therapy. *Nano Lett.* **2011**, *11*, 2560–2566.
- (22) Routzahn, A. L.; White, S. L.; Fong, L.-K.; Jain, P. K. Plasmonics with Doped Quantum Dots. *Isr. J. Chem.* **2012**, *52*, 983–991.
- (23) Buonsanti, R.; Milliron, D. J. Chemistry of Doped Colloidal Nanocrystals. *Chem. Mater.* **2013**, *25*, 1305–1317.
- (24) Lounis, S. D.; Runnerstrom, E. L.; Llordes, A.; Milliron, D. J. Defect Chemistry and Plasmon Physics of Colloidal Metal Oxide Nanocrystals. *J. Phys. Chem. Lett.* **2014**, *5*, 1564–1574.
- (25) Kriegel, I.; et al. Tuning the Excitonic and Plasmonic Properties of Copper Chalcogenide Nanocrystals. *J. Am. Chem. Soc.* **2012**, *134*, 1583–1590.
- (26) Luther, J. M.; Jain, P. K.; Ewers, T.; Alivisatos, A. P. Localized Surface Plasmon Resonances Arising from Free Carriers in Doped Quantum Dots. *Nat. Mater.* **2011**, *10*, 361–366.
- (27) Scotognella, F.; et al. Plasmonics in heavily-doped semiconductor nanocrystals. *Eur. Phys. J. B* **2013**, *86*, 1–13.
- (28) Mattox, T. M.; Bergerud, A.; Agrawal, A.; Milliron, D. J. Influence of Shape on the Surface Plasmon Resonance of Tungsten Bronze Nanocrystals. *Chem. Mater.* **2014**, *26*, 1779–1784.
- (29) Manthiram, K.; Alivisatos, A. P. Tunable Localized Surface Plasmon Resonances in Tungsten Oxide Nanocrystals. *J. Am. Chem. Soc.* **2012**, *134*, 3995–3998.
- (30) Gordon, T. R.; et al. Shape-Dependent Plasmonic Response and Directed Self-Assembly in a New Semiconductor Building Block, Indium-Doped Cadmium Oxide (ICO). *Nano Lett.* **2013**, *13*, 2857–2863.
- (31) Farvid, S. S.; Radovanovic, P. V. Phase Transformation of Colloidal In₂O₃ Nanocrystals Driven by the Interface Nucleation Mechanism: A Kinetic Study. *J. Am. Chem. Soc.* **2012**, *134* (16), 7015–7024.
- (32) Lee, J.; Petruska, M. A.; Sun, S. Surface Modification and Assembly of Transparent Indium Tin Oxide Nanocrystals for Enhanced Conductivity. *J. Phys. Chem. C* **2014**, *118*, 12017–12021.
- (33) Buonsanti, R.; Llordes, A.; Aloni, S.; Helms, B. A.; Milliron, D. J. Tunable Infrared Absorption and Visible Transparency of Colloidal Aluminum-Doped Zinc Oxide Nanocrystals. *Nano Lett.* **2011**, *11*, 4706–4710.
- (34) Choi, S.-I.; Nam, K. M.; Park, B. K.; Seo, W. S.; Park, J. T. Preparation and Optical Properties of Colloidal, Monodisperse, and Highly Crystalline ITO Nanoparticles. *Chem. Mater.* **2008**, *20*, 2609–2611.
- (35) Kanehara, M.; Koike, H.; Yoshinaga, T.; Teranishi, T. Indium Tin Oxide Nanoparticles with Compositionally Tunable Surface Plasmon Resonance Frequencies in the Near-IR Region. *J. Am. Chem. Soc.* **2009**, *131*, 17736–17737.
- (36) Dorfs, D.; et al. Reversible Tunability of the Near-Infrared Valence Band Plasmon Resonance in Cu₂-xSe Nanocrystals. *J. Am. Chem. Soc.* **2011**, *133*, 11175–11180.
- (37) Garcia, G.; et al. Dynamically Modulating the Surface Plasmon Resonance of Doped Semiconductor Nanocrystals. *Nano Lett.* **2011**, *11*, 4415–4420.
- (38) Llordes, A.; Garcia, G.; Gazquez, J.; Milliron, D. J. Tunable near-Infrared and Visible-Light Transmittance in Nanocrystal-in-Glass Composites. *Nature* **2013**, *500*, 323–326.
- (39) Runnerstrom, E. L.; Llordes, A.; Lounis, S. D.; Milliron, D. J. Nanostructured Electrochromic Smart Windows: Traditional Materials and NIR-Selective Plasmonic Nanocrystals. *Chem. Commun.* **2014**, *50*, 10555–10572.
- (40) Mendelsberg, R. J. et al. *Plasmonic Nanocrystal Sensors that Optically Track (Bio)Chemical Redox Reactions with Single-Electron Sensitivity*, submitted.
- (41) Schimpf, A. M.; Lounis, S. D.; Runnerstrom, E. L.; Milliron, D. J.; Gamelin, D. R. Redox Chemistries and Plasmon Energies of Photodoped In₂O₃ and Sn-Doped In₂O₃ (ITO) Nanocrystals. *J. Am. Chem. Soc.* **2015**, *137*, 518–524.
- (42) Mendelsberg, R. J.; Zhu, Y.; Anders, A. Determining the Nonparabolicity Factor of the CdO Conduction Band Using Indium Doping and the Drude Theory. *J. Phys. Appl. Phys.* **2012**, *45*, 425302.
- (43) Zhu, Y.; Mendelsberg, R. J.; Zhu, J.; Han, J.; Anders, A. Dopant-Induced Band Filling and Bandgap Renormalization in CdO: In Films. *J. Phys. Appl. Phys.* **2013**, *46*, 195102.
- (44) Mendelsberg, R. J.; Garcia, G.; Milliron, D. J. Extracting Reliable Electronic Properties from Transmission Spectra of Indium Tin Oxide Thin Films and Nanocrystal Films by Careful Application of the Drude Theory. *J. Appl. Phys.* **2012**, *111*, 063515.
- (45) Kriegel, I.; et al. Shedding Light on Vacancy-Doped Copper Chalcogenides: Shape-Controlled Synthesis, Optical Properties, and Modeling of Copper Telluride Nanocrystals with Near-Infrared Plasmon Resonances. *ACS Nano* **2013**, *7*, 4367–4377.
- (46) Draine, B. T.; Flatau, P. J. Discrete-Dipole Approximation For Scattering Calculations. *J. Opt. Soc. Am. A* **1994**, *11*, 1491–1499.
- (47) Flatau, P. J.; Draine, B. T. Fast near field calculations in the discrete dipole approximation for regular rectilinear grids. *Opt. Express* **2012**, *20*, 1247–1252.
- (48) Hooshmand, N.; Bordley, J. A.; El-Sayed, M. A. Are Hot Spots between Two Plasmonic Nanocubes of Silver or Gold Formed between Adjacent Corners or Adjacent Facets? A DDA Examination. *J. Phys. Chem. Lett.* **2014**, *5*, 2229–2234.
- (49) González, A. L.; Noguez, C. Optical Properties of Silver Nanoparticles. *Phys. Status Solidi C* **2007**, *4*, 4118–4126.
- (50) Gonzalez, A. L.; Noguez, C. Influence of Morphology on the Optical Properties of Metal Nanoparticles, 2006 (<http://arxiv.org/abs/physics/0609015>).
- (51) Jefferson, P. H.; et al. Bandgap and Effective Mass of Epitaxial Cadmium Oxide. *Appl. Phys. Lett.* **2008**, *92*, 022101.
- (52) Wu, J.; et al. Effects of the Narrow Band Gap on the Properties of InN. *Phys. Rev. B* **2002**, *66*, 201403.
- (53) Bohren, C. F.; Huffman, D. R. *Absorption and Scattering of Light by Small Particles*; Wiley: Hoboken, NJ, 2007.
- (54) Stiegler, J. M.; et al. Nanoscale Infrared Absorption Spectroscopy of Individual Nanoparticles Enabled by Scattering-Type Near-Field Microscopy. *ACS Nano* **2011**, *5*, 6494–6499.
- (55) Notarianni, M.; et al. Plasmonic Effect of Gold Nanoparticles in Organic Solar Cells. *Sol. Energy* **2014**, *106*, 23–37.
- (56) Manna, L.; Milliron, D. J.; Meisel, A.; Scher, E. C.; Alivisatos, A. P. Controlled Growth of Tetrapod-Branched Inorganic Nanocrystals. *Nat. Mater.* **2003**, *2*, 382–385.
- (57) Milliron, D. J.; et al. Colloidal Nanocrystal Heterostructures with Linear and Branched topology. *Nature* **2004**, *430*, 190–195.
- (58) Peng, X.; et al. Shape Control of CdSe Nanocrystals. *Nature* **2000**, *404*, 59–61.
- (59) Li, W.; et al. CuTe Nanocrystals: Shape and Size Control, Plasmonic Properties, and Use as SERS Probes and Photothermal Agents. *J. Am. Chem. Soc.* **2013**, *135*, 7098–7101.
- (60) Cobley, C. M.; Skrabalak, S. E.; Campbell, D. J.; Xia, Y. Shape-Controlled Synthesis of Silver Nanoparticles for Plasmonic and Sensing Applications. *Plasmonics* **2009**, *4*, 171–179.
- (61) Chen, H.; Kou, X.; Yang, Z.; Ni, W.; Wang, J. Shape- and Size-Dependent Refractive Index Sensitivity of Gold Nanoparticles. *Langmuir* **2008**, *24*, 5233–5237.
- (62) Zhang, S.; Bao, K.; Halas, N. J.; Xu, H.; Nordlander, P. Substrate-Induced Fano Resonances of a Plasmonic Nanocube: A Route to Increased-Sensitivity Localized Surface Plasmon Resonance Sensors Revealed. *Nano Lett.* **2011**, *11*, 1657–1663.

- (63) Haes, A. J.; Zou, S.; Zhao, J.; Schatz, G. C.; Van Duyne, R. P. Localized Surface Plasmon Resonance Spectroscopy near Molecular Resonances. *J. Am. Chem. Soc.* **2006**, *128*, 10905–10914.
- (64) Aroca, R. F.; Ross, D. J.; Domingo, C. Surface-Enhanced Infrared Spectroscopy. *Appl. Spectrosc.* **2004**, *58*, 324A–338A.
- (65) Zuloaga, J.; Prodan, E.; Nordlander, P. Quantum Description of the Plasmon Resonances of a Nanoparticle Dimer. *Nano Lett.* **2009**, *9*, 887–891.
- (66) Govorov, A. O.; et al. Gold Nanoparticle Ensembles As Heaters and Actuators: Melting and Collective Plasmon Resonances. *Nanoscale Res. Lett.* **2006**, *1*, 84–90.
- (67) Baffou, G.; Quidant, R.; Girard, C. Heat Generation in Plasmonic Nanostructures: Influence of Morphology. *Appl. Phys. Lett.* **2009**, *94*, 153109.
- (68) Arnida; Malugin, A.; Ghandehari, H. Cellular Uptake and Toxicity of Gold Nanoparticles in Prostate Cancer Cells: A Comparative Study of Rods and Spheres. *J. Appl. Toxicol.* **2010**, *30*, 212–217.
- (69) Kayal, S.; Ramanujan, R. V. Anti-Cancer Drug Loaded Iron-Gold Core-Shell Nanoparticles (Fe@Au) for Magnetic Drug Targeting. *J. Nanosci. Nanotechnol.* **2010**, *10*, 5527–5539.
- (70) Niu, L.; et al. Sensitivity Improved Plasmonic Gold Nanoholes Array Biosensor by Coupling Quantum-Dots for the Detection of Specific Biomolecular Interactions. *Biosens. Bioelectron.* **2013**, *50*, 137–142.